Journal of Materials Chemistry A

Materials for energy and sustainability

rsc.li/materials-a

ROYAL SOCIETY
OF CHEMISTRY

PAPER
Fan Fu *et al.*
Triple-cation perovskite solar cells fabricated by a hybrid
PVD/blade coating process using green solvents

PAPER

Check for updates

Triple-cation perovskite solar cells fabricated by a hybrid PVD/blade coating process using green solvents†

Severin Siegrist, [ID] Shih-Chi Yang, Evgeniia Gilshtein, [ID] Xiaoxiao Sun, Ayodhya N. Tiwari and Fan Fu [ID] *

The scalability of highly efficient organic–inorganic perovskite solar cells (PSCs) is one of the major challenges of solar module manufacturing. Various scalable methods have been explored to strive for uniform perovskite films of high crystal quality on large-area substrates, but each of these methods has individual limitations on the potential of successful commercialization of perovskite photovoltaics. Here, we report a fully scalable hybrid process, which combines vapor- and solution-based techniques to deposit high quality uniform perovskite films on large-area substrates. This two-step process does not use toxic solvents, and it further allows easy implementation of passivation strategies and additives. We fabricate PSCs based on this process and use blade coating to deposit a SnO_2 electron transporting layer and Spiro-OMeTAD hole transporting layer without halogenated solvents in ambient air. The fabricated PSCs have achieved open-circuit voltage up to 1.16 V and power conversion efficiency of 18.7% with good uniformity on 5 cm × 5 cm substrates.

Introduction

Organic–inorganic halide perovskite solar cells (PSCs) have shown tremendous advancements in the past ten years, now reaching certified power conversion efficiency (PCE) of 25.5%,[1] which is close to the record efficiency of crystalline silicon solar cells (26.7%).[2] This rapid development can be mainly attributed to the excellent optoelectronic properties of the perovskite material, which include high optical absorption coefficients, long carrier diffusion lengths, high charge carrier mobility, and to the development of facile perovskite fabrication methods due to the extraordinary defect tolerance of perovskites.[3–8] Furthermore, by changing the chemical composition of the perovskite compound, the optical band gap can be tuned broadly for tandem device applications,[9] such as perovskite/c-Si,[10–12] perovskite/CIGS[13–15] and all-perovskite tandems.[16,17]

One of the major challenges towards successful commercialization of perovskite photovoltaics is the fabrication of every layer of the PSC by scalable deposition methods and demonstration of high performance devices on a large area. At present, the perovskite layer of most efficient PSCs is fabricated by spin coating and using an anti-solvent dripping method to obtain compact, pinhole-free perovskite layers of high optoelectronic quality.[18–21] However, spin coating is not cost-effective due to its high solution waste, as up to 90% of the dripped solution can be ejected during spinning.[22] Moreover, films fabricated by spin coating are not uniform from the center to the corner, which exaggerates for large-area substrates (>10 cm × 10 cm).[23] Ultimately, spin coating is not suitable for large area in-line and continuous roll-to-roll (R2R) high throughput production processes. Thus, it is desirable to develop alternative scalable deposition methods for scaling up the perovskite photovoltaics.[23,24]

In recent years, several industrially scalable deposition methods have been developed to deposit uniform perovskite films on large-area substrates, which are compatible with high throughput productions. Generally, these scalable deposition methods can be divided into solution- and vapor-based techniques. Solution-based methods, such as blade coating,[25,26] slot-die coating,[27,28] inkjet printing,[1,29] and spray coating,[30] offer the possibility to mix additives into the precursor solution to control the film formation and enhance the morphology.[21,31] Moreover, various passivation strategies that are essential for improved efficiency and stability can be easily implemented as well.[32] Among the solution-based methods, blade coating is a promising, scalable technique due to its excellent material usage rate (~95%) and high throughput capabilities.[33] Over the past few years, Huang's group has developed various strategies to improve the film uniformity over large areas as well as the device performance, including compositional engineering,[34]

26680 | *J. Mater. Chem. A*, 2021, **9**, 26680–26687

This journal is © The Royal Society of Chemistry 2021

surfactants,[31] dopants,[35] additives,[32] and solvents.[36] Recently, the same group discovered a substantial void fraction in the buried perovskite/hole transporting layer interface induced by trapped dimethyl sulfoxide (DMSO) during film formation. The interfacial void fraction was reduced by partially substituting DMSO with solid-state carbohydrazide to achieve 23.6% efficient p–i–n PSC and 19.2% efficient mini-module with an aperture area of 50 cm^2 by blade coating.[37] However, to dissolve the inorganic halide precursors, solvents like 2-methoxyethanol (2-ME) or alternatively, N,N-dimethylformamide (DMF) are usually used.[8,36] These solvents (2-ME, DMF) have been known for their reproductive toxicity (Category 1B, H360), bearing risk to workers and the environment.[39–41] Moreover, it is challenging to form conformal films on rough surfaces, needed for monolithically integrated perovskite/silicon or perovskite/CIGS tandem solar cells.[12,42] These drawbacks could be overcome[38] by using vapor-based techniques.[43,44] These solvent-free techniques could conformally coat on non-planar surfaces over large-area substrates.[45] For example, Li *et al.* co-evaporated methylammonium iodide (MAI) and lead iodide (PbI$_2$) to obtain PSCs with PCE of 20.28% for a 0.16 cm^2 small-area device and 18.13% for a 21 cm^2 perovskite mini-module.[46] Liu *et al.* sequentially evaporated PbI$_2$, formamidinium iodide (FAI) and cesium iodide (CsI) to fabricate uniform and high quality perovskite films on glass (400 cm^2) and flexible (300 cm^2) substrates.[47] The small-area (0.09 cm^2) devices on the rigid substrate achieved PCEs between 19.50 and 20.50%. Although the uniformity of vapor-based techniques is impressive, it is very challenging to implement passivation strategies or controlling the perovskite composition that is essential for high performance and superior stability.[48]

In this work, we report a novel and scalable fabrication process of the perovskite film that combines the merits of the scalable solution- and vapor-based deposition methods, including facile compositional engineering to broadly tune the bandgap, and more importantly the avoidance of using toxic solvents. This hybrid process is composed of three steps. First, the inorganic halide precursors are sequentially deposited by solvent-free, physical vapor deposition (PVD). Next, the mixed solution of organic halide precursors in isopropanol is blade coated onto the heated inorganic halide template to obtain the perovskite film in ambient air, followed by thermal annealing to promote grain growth. We systematically vary the processing conditions of the perovskite absorber to gain insights into the perovskite formation mechanism during the PVD/blade coating process. Furthermore, in conjunction with blade coated charge transporting layers (SnO$_2$ and Spiro-OMeTAD), the optimized devices achieved high open-circuit voltage (V_{OC}) up to 1.16 V for a perovskite with an optical band gap of 1.56 eV and a PCE up to 18.7%, which is the highest reported efficiency of solution-based PSCs using green solvents only.

Hybrid PVD/blade coating fabrication process for scalable perovskite films

Fig. 1a shows the schematic of the scalable PVD/blade coating process to fabricate the perovskite layer. This hybrid process is

Fig. 1 Hybrid PVD/blade coating process for perovskite layers and morphology after each step. (a) Schematic of the three steps of the PVD/blade coating fabrication process. SEM top and cross-section view images after each fabrication step: (b) and (e) after evaporation, (c) and (f) after blade coating and (d) and (g) after thermal annealing. The scale bar is 500 nm.

composed of three steps. In the first step, the inorganic halide template is sequentially deposited by thermal evaporation on transparent conducting oxide coated substrates with an electron transporting layer (SnO_2). This template consists of a 300 nm thick lead iodide (PbI_2) layer on top of a 15 nm thin cesium iodide (CsI) layer. In the second step, the organic halide precursor solution, composed of formamidinium iodide (FAI), methylammonium bromide (MABr), and methylammonium chloride (MACl) dissolved in isopropanol, is blade coated on the inorganic halide template at a substrate temperature of 65 °C. In the last step, thermal annealing at 150 °C for 15 min is performed in ambient air to promote crystal growth to reduce the grain boundaries and to obtain a compact perovskite film with a large grain size. For the studies on the film formation and composition as well as for the fabrication of PSCs, we use the n–i–p architecture with blade coated tin oxide (SnO_2) as the underlying electron transporting layer.

Morphology and crystallinity of the perovskite film

In Fig. 1b–g, scanning electron microscopy (SEM) images depict the film morphology after each step of the PVD/blade coating process. Additionally, we provide SEM images of CsI layer to unveil its morphology in Fig. S1.† As shown in Fig. 1b the evaporated PbI_2 layer is composed of mixed rounded and elliptical plate-shaped grains of around 30 nm to 120 nm size. The cross-section view (Fig. 1e) shows the layer stack with PbI_2 (300 nm), CsI (15 nm), SnO_2 (35 nm) and hydrogenated indium oxide (IOH, 480 nm). The inorganic halide template has a smooth and uniform morphology, which is beneficial for pinhole-free perovskite films.[49] The XRD pattern in Fig. S2† shows a sharp diffraction peak at 12.7°, which corresponds to PbI_2.[50] After blade coating the organic halide solution, the PbI_2 peak decreases and simultaneously, a new diffraction peak at 14.1° emerges, indicating α-phase perovskite even before thermal annealing. Fig. 1c shows the SEM top view of the as-deposited perovskite film, subsequently after the blade coating step. The perovskite grains have a diameter between 100 and 500 nm without voids. The cross-section view (Fig. 1f) shows lots of small grains and the perovskite thickness is approximately twice the thickness of the inorganic halide template.[52] After thermal annealing, the grain growth is promoted and it results in large crystal grains and reduced grain boundaries (Fig. 1d).[53] In the cross-section view image, the perovskite thickness is unchanged and the surface morphology shows similar roughness to that prior to annealing (Fig. 1g). We further conducted atomic force microscopy (AFM) to quantify the surface roughness of the film after each step (see Fig. S3†). The root mean square roughness (R_q) of the film surface after PVD was calculated to be 8.76 nm (area of 5×5 μm^2), 30.2 nm after blade coating, and 34.7 nm after thermal annealing. These results agree well with the SEM images.

Perovskite film formation mechanism

For two-step methods with compact inorganic template layers (Fig. 2b), obtaining a compact and fully converted perovskite film depends on the processing method and conditions.[49,51] For this work, we focus on the processing conditions of the second step – the blade coating. We systematically investigate the organic halide concentration, blade coating speed and substrate temperature to elucidate the influence of these parameters on the perovskite formation mechanism. For these investigations, we fix the gap between the blade and the substrate to 100 μm. First, we use solutions of organic halide precursors (FAI/MABr/MACl) of different concentrations ranging from 10/1/1 to 90/9/9 mg mL^{-1}, while maintaining the substrate temperature at 65 °C and the speed at 30 mm s^{-1}. The results are shown in Fig. 2 and S4.†

For the solutions of low concentration, 10/1/1 mg mL^{-1} (Fig. S4a†) and 30/3/3 mg mL^{-1} (Fig. 2a and S4a†), the highest diffraction peaks correspond to PbI_2 (◆), while only tiny peaks can be detected that indicate α-phase perovskite. While the film obtained using 10/1/1 mg mL^{-1} appears yellowish, the film using 30/3/3 mg mL^{-1} is brownish, indicating a higher degree of perovskite conversion (Fig. S4b and c†). For both concentrations, we observe that perovskite has formed in the upper region of the film, whereas residual PbI_2 is located in the lower region. This perovskite capping layer inhibits further diffusion of organic cations and iodide as well as their reaction with the buried PbI_2 (Fig. S5a†),[54,55] leading to thinner films (as for higher concentrations). We further spotted bright dots at the grain boundaries (Fig. 2e), which we relate to remnant PbI_2. When we use concentrations between 50/5/5 mg mL^{-1} and 70/7/7 mg mL^{-1}, the film has converted to perovskite, appearing dark brown (Fig. S4d–f†). However, XRD and SEM still show a large amount of unreacted PbI_2 for 50/5/5 mg mL^{-1}, while for 60/6/6 mg mL^{-1} these residues have almost reacted and converted to a compact perovskite layer (Fig. 2f, g and S4e†). We suggest that during the coalescence of perovskite grains, residual PbI_2 that is trapped between adjacent perovskite grains reacts with the dissolved organic halide precursors to perovskite and prevents the formation of voids (Fig. S5b†). Using 70/7/7 mg mL^{-1}, the perovskite crystallinity increases and voids are formed (Fig. S4f†). Further increasing the concentration to 90/9/9 mg mL^{-1} leads to very rough films of large crystal grains (Fig. 2h, i and S4g†). We spot gray dots on the crystal grain surface, which we relate to crystallized organic halides. Furthermore, voids in the bulk and between adjacent grains have formed as no PbI_2 was available during coalescence (Fig. S5c†). Additionally, a new diffraction peak appears at 11.8°, indicating a hexagonal perovskite δ-phase (Fig. 2a)[56] making this perovskite film inappropriate for PSC devices.

Next, we used different speeds from 1 mm s^{-1} to 90 mm s^{-1} and blade coated the organic halide solution on the inorganic halide template, while maintaining the substrate temperature at 65 °C and the concentration at 60/6/6 mg mL^{-1} (Fig. S6†). For blade coating, two coating regimes exist, the evaporation regime and the Landau–Levich regime.[31] In the evaporation regime (speed ≤ 10 mm s^{-1}), slower coating speed yields thicker layers, *i.e.*, a higher amount of organic halide precursors is supplied due to the increased residence time per unit length. Therefore, the diffraction peak of PbI_2 decreases with reduced speed (1 mm s^{-1}) and the perovskite peak intensity of (110) increases

26682 | *J. Mater. Chem. A*, 2021, **9**, 26680–26687

This journal is © The Royal Society of Chemistry 2021

Fig. 2 Evaporated inorganic halide template and perovskite films prepared using 30/3/3 mg mL^{-1}, 60/6/6 mg mL^{-1} and 90/9/9 mg mL^{-1} of FAI/MABr/MACl organic halide precursor solution concentration. (a) XRD patterns (log-scale) with indicated diffraction peaks of the α-phase perovskite crystal planes. PbI$_2$ is labeled with a ◆ and IOH with a *. (b)–(i) SEM cross-section and top view images of (b) and (c) inorganic halide template and perovskite films prepared with different concentrations of the organic halide precursors: (d) and (e) 30/3/3 mg mL^{-1}, (f) and (g) 60/6/6 mg mL^{-1} and (h) and (i) 90/9/9 mg mL^{-1} of FAI/MABr/MACl. The scale bar is 500 nm.

compared to 10 mm s^{-1} (Fig. S6a†). The higher perovskite conversion degree can also be observed from the lower transparency of the sample pictures in background illumination mode (Fig. S6b and c†). However, we obtain incomplete perovskite conversion in the evaporation regime. With coating speeds >10 mm s^{-1}, the Landau–Levich regime is reached, where viscous forces become dominant, dragging more solution on the substrate with increasing speed.[22] Hence, the degree of perovskite conversion increases with increasing speed. Using a speed of 30 mm s^{-1}, a compact perovskite film with remnant PbI$_2$ is obtained (Fig. S6d†). The sample shows a uniform coating. With a coating speed ≥50 mm s^{-1}, no remnant PbI$_2$ can be detected and the film uniformity is lost. At 50 mm s^{-1}, we observe the formation of voids in the perovskite bulk (Fig. S6e†) and the emergence of a diffraction peak at 11.8°, which indicates δ-phase perovskite (Fig. S6a†). Interestingly, this δ-phase perovskite has been formed immediately after blade coating at 65 °C. Further increasing the speed results in large and coarse crystal grains with high crystallinity (Fig. S6f and g†).

As a consequence, we investigated the influence of different substrate temperatures on the perovskite formation mechanism (Fig. S7†), ranging from 25 °C to 75° (boiling point of isopropanol: 82.5 °C). We maintained the coating speed at 30 mm s^{-1} and used a concentration of 60/6/6 mg mL^{-1}. For low substrate temperatures ≤40 °C, complete perovskite conversion

is obtained, enabled by the slower drying rate. However, the complete conversion comes at the expense of uniformity due to the coffee-ring effect, which also leads to regions of perovskite δ-phase (see the gray area in Fig. S7b and c†). With 55 °C substrate temperature or higher, the coffee-ring effect can be minimized, resulting in uniform coatings. A substrate temperature of 65 °C shows the highest degree of perovskite while maintaining uniformity and high crystallinity (Fig. S7e†). At 75 °C, we observe decreasing perovskite conversion, as the PbI$_2$ diffraction peak increases again. In Fig. S7f,† we also detected remnant PbI$_2$ on the surface of the perovskite film, meaning that the drying rate was too high, interrupting the perovskite conversion on the surface.

To sum up our findings, the perovskite film blade coated with 70 mm s^{-1} at 65 °C with an organic halide concentration of 60/6/6 mg mL^{-1} of FAI/MABr/MACl is presented, in Fig. S8,† showing three different regions. We identify these regions as δ-phase perovskite (Fig. S8d,† red), transition (Fig. S8e,† orange) and α-phase perovskite (Fig. S8f,† green) and provide SEM cross-section and top view images for the morphologies. In summary, we have shown that the organic halide precursor concentration, the coating speed and the substrate temperature play important roles in obtaining uniform and converted perovskite films by the PVD/blade process. It is essential to balance the organic and inorganic halide precursors by

This journal is © The Royal Society of Chemistry 2021

J. Mater. Chem. A, 2021, **9**, 26680–26687 | **26683**

Fig. 3 ToF-SIMS depth profile of (a)–(c) cation species at different stages of the hybrid PVD/blade coating process and XPS with depth profiling (d)–(f) of the stack after each step of the coating process. XPS Cs 3d spectra after (a) evaporation, (b) blade coating and (c) annealing. The ten lines correspond to profiles at 0 nm, 10 nm, 20 nm, 30 nm, 40 nm, 80 nm, 120 nm, 160 nm, 200 nm and 300 nm depth.

controlling the processing conditions and selecting an appropriate drying rate to suppress the coffee-ring effect.

Next, we perform depth profiling using time-of-flight secondary ion mass spectroscopy (ToF-SIMS) and X-ray photoelectron spectroscopy (XPS) to shed light on the film composition and the cationic interdiffusion process.

Fig. 3 shows the depth profiles obtained by ToF-SIMS and XPS after each step of the PVD/blade coating process. The ToF-SIMS uses an oxygen sputter gun to detect the positive ion species (Fig. 3a–c). After thermal evaporation, the bilayer inorganic template can be clearly differentiated. First, a constant signal of Pb^+ ions (up to 100 s sputter time) is detected, representing the PbI_2 layer. Second, a peak of Cs^+ ions follows (between 100 and 125 s), indicating the CsI layer, meanwhile the Pb cation signal decreases substantially (Fig. 3a). This agrees well with XPS Cs 3d spectra after PVD (Fig. 3d). The first peaks are detected at a sample depth of 300 nm. After blade coating, a uniform signal of Cs cations is detected across the as-deposited film, which shows that Cs species have already diffused throughout the layer (Fig. 3b). This finding is also supported by XPS in Fig. 3e. After thermal annealing, ToF-SIMS and XPS show comparable results to those after blade coating, which means that perovskite conversion is completed after blade coating and Cs species have diffused uniformly into the perovskite film (Fig. 3c, f and S9†). The subsequent thermal annealing in the PVD/blade coating process finally induces grain growth to reduce the grain boundaries, which is beneficial for the optoelectronic properties.

Optoelectronic properties of the perovskite film

To evaluate the optoelectronic properties of our perovskite film fabricated by PVD/blade, we also fabricated perovskite films by two-step spin coating (spin + spin). To exclude the effect of any charge extraction layer, we deposited the perovskite films directly on quartz substrates. We have shown in Note S1† that the morphology of the evaporated inorganic halide template remains unchanged when using different amorphous substrates.[57] Fig. S10a† summarizes the absorbance and the photoluminescence spectra of the perovskite film on a quartz substrate for both fabrication methods (PVD + blade and spin + spin). In Fig. S11,† we provide Tauc plots of these perovskite films and estimated the optical bandgap with a linear fit to be 1.56 eV for both absorbers.[58] We further investigated the charge recombination dynamics by steady-state photoluminescence (PL) and time-resolved photoluminescence (TRPL) decay measurements.[60] The PL peaks are located at 794 nm (1.56 eV) for both perovskite films. The PL intensity is highest for the perovskite film by PVD/blade, which indicates stronger suppression of non-radiative recombination processes compared to two-step spin coating. Fig. S10b† shows the TRPL decays of the perovskite films by different fabrication methods. We fit the decays with the bi-exponential function:

$$I(t) = A_1 \exp\left(-\frac{t}{\tau_1}\right) + A_2 \exp\left(-\frac{t}{\tau_2}\right)$$

and obtain two decay times, the fast decay lifetime τ_1 and the slow decay lifetime τ_2.[59,61] The fitting parameters are provided in Table S1.† The charge carrier lifetimes are comparably long for both perovskite films by PVD/blade (343 ns and 1406 ns) and spin + spin (396 ns and 1148 ns), showing that perovskite films fabricated by PVD/blade achieve comparable crystal quality and photovoltaic performance (Fig. S12†).

Photovoltaic performance of PSCs by PVD/blade

To evaluate the photovoltaic performance of perovskite films fabricated by PVD/blade, we fabricated n–i–p PSCs with layer stack IOH/SnO$_2$/perovskite/Spiro-OMeTAD/Au on 5 cm × 5 cm substrates. We blade coated both charge transporting layers in ambient air and used non-toxic solvents for both layers, namely de-ionized water for SnO$_2$ and p-xylene for spiro-OMeTAD.[62] To passivate the perovskite layer, we used phenethylammonium iodide (PEAI).[20] Fig. 4a shows a SEM cross-section image of the sample with remnant PbI$_2$, confirmed by XRD (Fig. S13†). J–V measurement of the champion device reveals negligible

hysteresis with an open-circuit voltage (V_{OC}) of 1.11 V, a short-current density (J_{SC}) of 23.31 mA cm^{-2} and a fill factor (FF) of 72.00%, resulting in a PCE of 18.66% (Fig. 4b). The maximum power point (MPP) tracking yields 17.74 mW cm^{-2} after 30 s (Fig. 4c). This is the highest value for scalable PSCs with green solvents (Fig. 4d). To check the uniformity of our process, we provide photovoltaic performance statistics of 34 cells on 5 cm × 5 cm substrates (Fig. S14†). On average, we obtained a V_{OC} of around 1.13 V and J_{SC} of 21 mA cm^{-2}. The best device showed V_{OC} of 1.16 V for a bandgap of 1.56 eV, being only limited by FF and J_{SC}. The external quantum efficiency (EQE) measurement yields an integrated J_{SC} value of 21.86 mA cm^{-2}, showing further scope of improvement in the light management (Fig. S15†).

In conclusion, we have reported a new and scalable hybrid perovskite fabrication process, combining thermal evaporation and blade coating using non-toxic solvents. We systematically investigated the influence of processing parameters on the perovskite formation mechanism during the PVD/blade process and elucidated the growth mechanism. We used such perovskite absorbers together with ambient air-processed, blade coated charge transporting layers to fabricate scalable PSCs
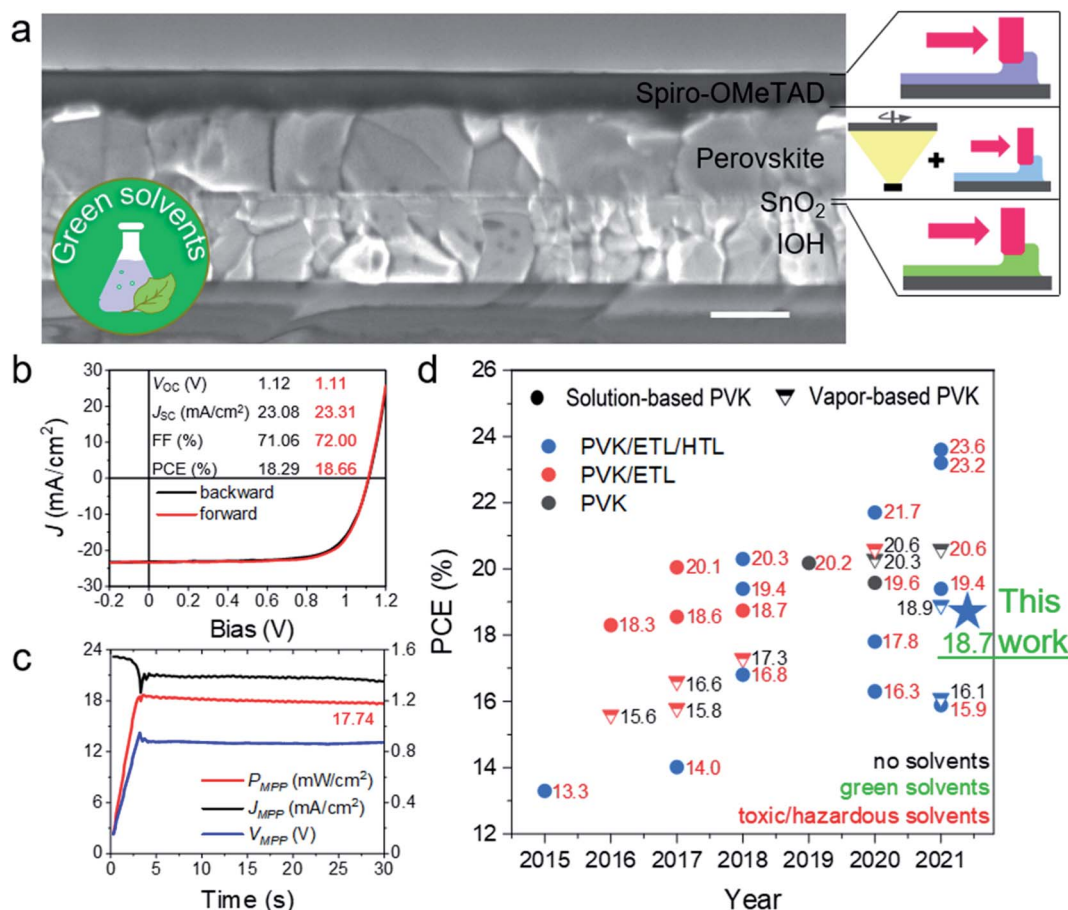
Fig. 4 (a) SEM cross-section view of PSC with blade coated charge transporting layers and perovskite layer by PVD/blade coating. The scale bar is 500 nm. (b) Current–voltage behavior and (c) MPP tracking of the champion device. (d) Power conversion efficiency *versus* year for selected, small-area (~0.1 cm^2) devices with indicated layers fabricated by scalable deposition methods (symbol color). Additionally, devices are distinguished by solution- and vapor-based perovskite absorber layers (symbol type) as well as by the use of green or toxic/hazardous solvents in the perovskite fabrication (font color). Perovskite: PVK, electron transporting layer: ETL and hole transporting layer: HTL.

This journal is © The Royal Society of Chemistry 2021

J. Mater. Chem. A, 2021, **9**, 26680–26687 | **26685**

with a V_{OC} of 1.16 V and PCE up to 18.7% using green solvents only. With our work, we make an important contribution to reduce the performance gap between toxic and green solvent-based, scalable perovskite fabrication. PVD/blade is a promising process to fabricate high quality perovskite layers on large-area substrates. It can allow a facile implementation of passivation strategies and additives into the precursor solution for blade coating. Additionally, it can be adapted for wide band gap perovskite films and be eventually applied to coat textured surfaces, *e.g.* in tandem solar cell applications. Moreover, other meniscus-guided deposition methods can replace blade coating, such as slot-die coating or inkjet printing. Overall, the proposed method and its variants are easily scalable for large area manufacturing while the avoidance of toxic solvents is an additional advantage for successful commercialization of the PSC technology. Besides, the processes can be applied on flexible foils as well, paving the way for roll-to-roll or sheet-to-sheet manufacturing in the future.

Conflicts of interest

The authors declare no competing financial interest.

Acknowledgements

References

1 M. A. Green and K. Emery, *Prog. Photovoltaics*, 1993, **1**(1), 25–29.
2 K. Yoshikawa, H. Kawasaki, W. Yoshida, T. Irie, K. Konishi, K. Nakano, T. Uto, D. Adachi, M. Kanematsu, H. Uzu and K. Yamamoto, *Nat. Energy*, 2017, **2**, 17032.
3 S. De Wolf, J. Holovsky, S. J. Moon, P. Löper, B. Niesen, M. Ledinsky, F. J. Haug, J. H. Yum and C. Ballif, *J. Phys. Chem. Lett.*, 2014, **5**(6), 1035–1039.
4 G. E. Eperon, S. D. Stranks, C. Menelaou, M. B. Johnston, L. M. Herz and H. J. Snaith, *Energy Environ. Sci.*, 2014, **7**(3), 982–988.
5 Q. Dong, Y. Fang, Y. Shao and J. Huang, *Science*, 2015, **347**(6225), 967–970.
6 M. V. Kovalenko, L. Protesescu and M. I. Bodnarchuk, *Science*, 2017, **358**(6364), 745–750.
7 W. J. Yin, T. Shi and Y. Yan, *Appl. Phys. Lett.*, 2014, **104**, 063903.
8 M. M. Lee, J. Teuscher, T. Miyasaka, T. N. Murakami and H. J. Snaith, *Science*, 2012, **338**(6107), 643–647.
9 R. K. Kothandaraman, Y. Jiang, T. Feurer, A. N. Tiwari and F. Fu, *Small Methods*, 2020, **4**(10), 1–56.
10 A. Al-Ashouri, E. Köhnen, B. Li, A. Magomedov, H. Hempel, P. Caprioglio, J. A. Márquez, A. B. M. Vilches, E. Kasparavicius, J. A. Smith, N. Phung, D. Menzel, M. Grischek, L. Kegelmann, D. Skroblin, C. Gollwitzer, T. Malinauskas, M. Jošt, G. Matič, B. Rech, R. Schlatmann, M. Topič, L. Korte, A. Abate, B. Stannowski, D. Neher, M. Stolterfoht, T. Unold, V. Getautis and S. Albrecht, *Science*, 2020, **370**(6522), 1300–1309.
11 B. Chen, S. W. Baek, Y. Hou, E. Aydin, M. De Bastiani, B. Scheffel, A. Proppe, Z. Huang, M. Wei, Y. K. Wang, E. H. Jung, T. G. Allen, E. Van Kerschaver, F. P. García de Arquer, M. I. Saidaminov, S. Hoogland, S. De Wolf and E. H. Sargent, *Nat. Commun.*, 2020, **11**, 1257.
12 F. Sahli, J. Werner, B. A. Kamino, M. Bräuninger, R. Monnard, B. Paviet-Salomon, L. Barraud, L. Ding, J. J. Diaz Leon, D. Sacchetto, G. Cattaneo, M. Despeisse, M. Boccard, S. Nicolay, Q. Jeangros, B. Niesen and C. Ballif, *Nat. Mater.*, 2018, **17**(9), 820–826.
13 A. Al-Ashouri, A. Magomedov, M. Roß, M. Jošt, M. Talaikis, G. Chistiakova, T. Bertram, J. A. Márquez, E. Köhnen, E. Kasparavičius, S. Levcenco, L. Gil-Escrig, C. J. Hages, R. Schlatmann, B. Rech, T. Malinauskas, T. Unold, C. A. Kaufmann, L. Korte, G. Niaura, V. Getautis and S. Albrecht, *Energy Environ. Sci.*, 2019, **12**(11), 3356–3369.
14 D. H. Kim, C. P. Muzzillo, J. Tong, A. F. Palmstrom, B. W. Larson, C. Choi, S. P. Harvey, S. Glynn, J. B. Whitaker, F. Zhang, Z. Li, H. Lu, M. F. A. M. van Hest, J. J. Berry, L. M. Mansfield, Y. Huang, Y. Yan and K. Zhu, *Joule*, 2019, **3**(7), 1734–1745.
15 F. Fu, T. Feurer, T. P. Weiss, S. Pisoni, E. Avancini, C. Andres, S. Buecheler and A. N. Tiwari, *Nat. Energy*, 2017, **2**, 16190.
16 K. Xiao, R. Lin, Q. Han, Y. Hou, Z. Qin, H. T. Nguyen, J. Wen, M. Wei, V. Yeddu, M. I. Saidaminov, Y. Gao, X. Luo, Y. Wang, H. Gao, C. Zhang, J. Xu, J. Zhu, E. H. Sargent and H. Tan, *Nat. Energy*, 2020, **5**(11), 870–880.
17 J. Tong, Z. Song, D. H. Kim, X. Chen, C. Chen, A. F. Palmstrom, P. F. Ndione, M. O. Reese, S. P. Dunfield, O. G. Reid, J. Liu, F. Zhang, S. P. Harvey, Z. Li, S. T. Christensen, G. Teeter, D. Zhao, M. M. Al-Jassim, M. F. A. M. Van Hest, M. C. Beard, S. E. Shaheen, J. J. Berry, Y. Yan and K. Zhu, *Science*, 2019, **364**(6439), 475–479.
18 M. Xiao, F. Huang, W. Huang, Y. Dkhissi, Y. Zhu, J. Etheridge, A. Gray-Weale, U. Bach, Y. B. Cheng and L. Spiccia, *Angew. Chem., Int. Ed.*, 2014, **53**(37), 9898–9903.
19 N. J. Jeon, J. H. Noh, Y. C. Kim, W. S. Yang, S. Ryu and S. I. Seok, *Nat. Mater.*, 2014, **13**(9), 897–903.
20 Q. Jiang, Y. Zhao, X. Zhang, X. Yang, Y. Chen, Z. Chu, Q. Ye, X. Li, Z. Yin and J. You, *Nat. Photonics*, 2019, **13**(7), 460–466.
21 J. Jeong, M. M. Kim, J. Seo, H. Lu, P. Ahlawat, A. Mishra, Y. Yang, M. A. Hope, F. T. Eickemeyer, M. M. Kim, Y. J. Yoon, I. W. Choi, B. P. Darwich, S. J. Choi, Y. Jo, J. H. Lee, B. Walker, S. M. Zakeeruddin, L. Emsley, U. Rothlisberger, A. Hagfeldt, D. S. Kim, M. Grätzel and J. Y. Kim, *Nature*, 2021, **592**, 381–385.
22 X. Gu, L. Shaw, K. Gu, M. F. Toney and Z. Bao, *Nat. Commun.*, 2018, **9**, 534.

26686 | *J. Mater. Chem. A*, 2021, **9**, 26680–26687

This journal is © The Royal Society of Chemistry 2021

23 Z. Li, T. R. Klein, D. H. Kim, M. Yang, J. J. Berry, M. F. A. M. Van Hest and K. Zhu, *Nat. Rev. Mater.*, 2018, **3**, 1–20.

24 D. Li, D. Zhang, K. S. Lim, Y. Hu, Y. Rong, A. Mei, N. G. Park and H. Han, *Adv. Funct. Mater.*, 2020, 2008621.

25 Y. Deng, E. Peng, Y. Shao, Z. Xiao, Q. Dong and J. Huang, *Energy Environ. Sci.*, 2015, **8**(5), 1544–1550.

26 S. Razza, F. Di Giacomo, F. Matteocci, L. Cinà, A. L. Palma, S. Casaluci, P. Cameron, A. D'Epifanio, S. Licoccia, A. Reale, T. M. Brown and A. Di Carlo, *J. Power Sources*, 2015, **277**, 286–291.

27 K. Hwang, Y. S. Jung, Y. J. Heo, F. H. Scholes, S. E. Watkins, J. Subbiah, D. J. Jones, D. Y. Kim and D. Vak, *Adv. Mater.*, 2015, **27**(7), 1241–1247.

28 D. Vak, K. Hwang, A. Faulks, Y. S. Jung, N. Clark, D. Y. Kim, G. J. Wilson and S. E. Watkins, *Adv. Energy Mater.*, 2015, **5**(4), 1–8.

29 Z. Wei, H. Chen, K. Yan and S. Yang, *Angew. Chem., Int. Ed.*, 2014, **53**(48), 13239–13243.

30 J. H. Heo, M. H. Lee, M. H. Jang and S. H. Im, *J. Mater. Chem. A*, 2016, **4**(45), 17636–17642.

31 Y. Deng, X. Zheng, Y. Bai, Q. Wang, J. Zhao and J. Huang, *Nat. Energy*, 2018, **3**(7), 560–566.

32 W. Q. Wu, Z. Yang, P. N. Rudd, Y. Shao, X. Dai, H. Wei, J. Zhao, Y. Fang, Q. Wang, Y. Liu, Y. Deng, X. Xiao, Y. Feng and J. Huang, *Sci. Adv.*, 2019, **5**(3), 1–10.

33 F. Di Giacomo, S. Shanmugam, H. Fledderus, B. J. Bruijnaers, W. J. H. Verhees, M. S. Dorenkamper, S. C. Veenstra, W. Qiu, R. Gehlhaar, T. Merckx, T. Aernouts, R. Andriessen and Y. Galagan, *Sol. Energy Mater. Sol. Cells*, 2018, **181**, 53–59.

34 S. Tang, Y. Deng, X. Zheng, Y. Bai, Y. Fang, Q. Dong, H. Wei and J. Huang, *Adv. Energy Mater.*, 2017, **7**(18), 1–7.

35 W. Q. Wu, Q. Wang, Y. Fang, Y. Shao, S. Tang, Y. Deng, H. Lu, Y. Liu, T. Li, Z. Yang, A. Gruverman and J. Huang, *Nat. Commun.*, 2018, **9**(1), 1–8.

36 Y. Deng, C. H. van Brackle, X. Dai, J. Zhao, B. Chen and J. Huang, *Sci. Adv.*, 2019, **5**(12), 1–9.

37 S. Chen, X. Dai, S. Xu, H. Jiao, L. Zhao and J. Huang, *Science*, 2021, **373**(6557), 902–907.

38 S. Chen, X. Xiao, H. Gu and J. Huang, *Sci. Adv.*, 2021, **7**(10), 1–7.

39 National Center for Biotechnology Information, 2-Methoxyethanol – PubChem Compound Summary for CID 8019, accessed Jun 18, 2021, https://pubchem.ncbi.nlm.nih.gov/compound/2-Methoxyethanol.

40 National Center for Biotechnology Information, N,N-Dimethylformamide – PubChem Compound Summary for CID 8019, accessed Jun 18, 2021, https://pubchem.ncbi.nlm.nih.gov/compound/6228.

41 N. G. Park, *Nature Sustainability*, 2021, **4**(3), 192–193.

42 M. Jošt, L. Kegelmann, L. Korte and S. Albrecht, *Adv. Energy Mater.*, 2020, **10**, 1904102.

43 C. Momblona, L. Gil-Escrig, E. Bandiello, E. M. Hutter, M. Sessolo, K. Lederer, J. Blochwitz-Nimoth and H. J. Bolink, *Energy Environ. Sci.*, 2016, **9**(11), 3456–3463.

44 J. Ávila, C. Momblona, P. P. Boix, M. Sessolo and H. J. Bolink, *Joule*, 2017, **1**(3), 431–442.

45 E. Köhnen, P. Wagner, F. Lang, A. Cruz, B. Li, M. Roß, M. Jošt, A. B. Morales-Vilches, M. Topič, M. Stolterfoht, D. Neher, L. Korte, B. Rech, R. Schlatmann, B. Stannowski and S. Albrecht, *Sol. RRL*, 2021, 2100244.

46 J. Li, H. Wang, X. Y. Chin, H. A. Dewi, K. Vergeer, T. W. Goh, J. W. M. Lim, J. H. Lew, K. P. Loh, C. Soci, T. C. Sum, H. J. Bolink, N. Mathews, S. Mhaisalkar and A. Bruno, *Joule*, 2020, **4**(5), 1035–1053.

47 J. Feng, Y. Jiao, H. Wang, X. Zhu, Y. Sun, M. Du, Y. Cao, D. Yang and S. (Frank) Liu, *Energy Environ. Sci.*, 2021, **14**(5), 3035–3043.

48 L. Gil-Escrig, C. Momblona, M. G. La-Placa, P. P. Boix, M. Sessolo and H. J. Bolink, *Adv. Energy Mater.*, 2018, **8**(14), 1–6.

49 J. Bing, S. Huang and A. W. Y. Ho-Baillie, *Energy Technol.*, 2020, **8**(4), 1–22.

50 T. J. Jacobsson, L. J. Schwan, M. Ottosson, A. Hagfeldt and T. Edvinsson, *Inorg. Chem.*, 2015, **54**(22), 10678–10685.

51 H. Ko, S. J. Yang, C. Park, D. H. Sin, H. Lee and K. Cho, *ACS Appl. Mater. Interfaces*, 2019, **11**(7), 7037–7045.

52 D. Liu, M. K. Gangishetty and T. L. Kelly, *J. Mater. Chem. A*, 2014, **2**(46), 19873–19881.

53 A. Ummadisingu and M. Grätzel, *Sci. Adv.*, 2018, **4**(2), 1–10.

54 Y. Fu, F. Meng, M. B. Rowley, B. J. Thompson, M. J. Shearer, D. Ma, R. J. Hamers, J. C. Wright and S. Jin, *J. Am. Chem. Soc.*, 2015, **137**(17), 5810–5818.

55 M. Chauhan, Y. Zhong, K. Schötz, B. Tripathi, A. Köhler, S. Huettner and F. Panzer, *J. Mater. Chem. A*, 2020, **8**(10), 5086–5094.

56 C. C. Stoumpos, C. D. Malliakas and M. G. Kanatzidis, *Inorg. Chem.*, 2013, **52**(15), 9019–9038.

57 F. Fu, L. Kranz, S. Yoon, J. Löckinger, T. Jäger, J. Perrenoud, T. Feurer, C. Gretener, S. Buecheler and A. N. Tiwari, *Phys. Status Solidi A*, 2015, **212**(12), 2708–2717.

58 A. R. Zanatta, *Sci. Rep.*, 2019, **9**(1), 11225.

59 Y. Yamada, T. Nakamura, M. Endo, A. Wakamiya and Y. Kanemitsu, *J. Am. Chem. Soc.*, 2014, **136**(33), 11610–11613.

60 T. Kirchartz, J. A. Márquez, M. Stolterfoht and T. Unold, *Adv. Energy Mater.*, 2020, **10**, 1904134.

61 K. Liu, Q. Liang, M. Qin, D. Shen, H. Yin, Z. Ren, Y. Zhang, H. Zhang, P. W. K. Fong, Z. Wu, J. Huang, J. Hao, Z. Zheng, S. K. So, C. S. Lee, X. Lu and G. Li, *Joule*, 2020, **4**(11), 2404–2425.

62 F. Isabelli, F. Di Giacomo, H. Gorter, F. Brunetti, P. Groen, R. Andriessen and Y. Galagan, *ACS Appl. Energy Mater.*, 2018, **1**(11), 6056–6063.

This journal is © The Royal Society of Chemistry 2021

J. Mater. Chem. A, 2021, **9**, 26680–26687 | **26687**